Investigation of the anomalous and topological Hall effects in layered monoclinic ferromagnet $Cr_{2.76}Te_4$

Shubham Purwar [1], Achintya Low,[1] Anumita Bose,[2] Awadhesh Narayan,[2] and S. Thirupathaiah [1,*]

[1]*Department of Condensed Matter and Materials Physics, S. N. Bose National Centre for Basic Sciences, Kolkata, West Bengal 700106, India*
[2]*Solid State and Structural Chemistry Unit, Indian Institute of Science, Bengaluru 560012, India*

We studied the electrical transport, Hall effect, and magnetic properties of monoclinic layered ferromagnet $Cr_{2.76}Te_4$. Our studies demonstrate $Cr_{2.76}Te_4$ to be a soft ferromagnet with strong magnetocrystalline anisotropy. Below 50 K, the system shows an antiferromagneticlike transition. Interestingly, between 50 and 150 K, we observe fluctuating magnetic moments between in-plane and out-of-plane orientations, leading to noncoplanar spin structure. On the other hand, the electrical resistivity data suggest it to be metallic throughout the measured temperature range, except a *kink* at around 50 K due to antiferromagnetic ordering. The Rhodes-Wohlfarth ratio $\frac{\mu_{\mathrm{eff}}}{\mu_s} = 1.89(>1)$ calculated from our magnetic studies confirms that $Cr_{2.76}Te_4$ is an itinerant ferromagnet. Large anomalous Hall effect has been observed due to the skew scattering of impurities and the topological Hall effect has been observed due to noncoplanar spin structure in the presence of strong magnetocrystalline anisotropy. We examined the mechanism of anomalous Hall effect by employing the first-principles calculations.

I. INTRODUCTION

Two-dimensional (2D) magnetic materials with topological properties [1–3] have sparked significant research attention recently due to their potential applications in spintronics and magnetic storage devices [4–6]. Importantly, these are the van der Waals (vdW) magnets possessing peculiar magnetic properties with strong magnetocrystalline anisotropy (MCA) [7–9]. In general, the Heisenberg-type ferromagnet does not exist with long-range magnetic ordering at a finite temperature in the 2D limit due to dominant thermal fluctuations [10]. However, the strong magnetic anisotropy that is usually present in the low-dimensional materials can stabilize the long-range magnetic ordering to become a 2D Ising-type ferromagnet [11]. To date, many 2D ferromagnets have been discovered experimentally [12,13], but only a few of them can show the topological signatures such as the topological Hall effect (THE) or skyrmion lattice. For instance, the recent microscopic studies on $Cr_2Ge_2Te_6$ [14], Fe_3GeTe_2 [15], and Fe_5GeTe_2 [16,17] demonstrated topological magnetic structure in the form of skymion bubbles in their low-dimensional form.

On the other hand, soon after predicting the layered Cr_xTe_y-type systems as potential candidates to realize the 2D ferromagnetism in their bulk form [18,19], a variety of Cr_xTe_y compounds were grown including CrTe [20], Cr_2Te_3 [21], Cr_3Te_4 [22], and Cr_5Te_8 [23]. Interestingly, all these systems are formed by the alternative stacking of Cr-full (CrTe$_2$ layer) and Cr-vacant (intercalated Cr layer) layers along either the *a* axis or the *c* axis [24]. Thus, the Cr concentration plays a critical role in forming the crystal structure,

magnetic, and transport properties. The compounds like Cr_5Te_8, Cr_2Te_3, and Cr_3Te_4 are reported to crystallize in monoclinic or trigonal structures, whereas $Cr_{1-x}Te$ ($x < 0.1$) crystallizes in the hexagonal NiAs-type structures [25]. The electronic band structure calculations performed on CrTe, Cr_2Te_3, and Cr_3Te_4 suggest a strong out-of-plane Cr $3d$ e_g orbital, $d_{z^2} - d_{z^2}$, overlapping along the *c* axis to have relatively smaller nearest-neighbor Cr-Cr distance [24]. In addition, Cr_5Te_8 [23], $Cr_{1.2}Te_2$ [26], and $Cr_{0.87}Te$ [27] are known to show topological properties in the hexagonal phase.

In this work, we systematically investigate the electrical transport, Hall effect, and magnetic properties of monoclinic $Cr_{2.76}Te_4$, which is very close to the stoichiometric composition of Cr_3Te_4. We observe that the easy axis of magnetization is parallel to the *bc* plane, leading to strong magnetocrystalline anisotropy. Below 50 K, the system shows antiferromagneticlike transition. In addition, we find fluctuating Cr magnetic moments between in-plane and out-of-plane directions within the temperature range of 50 and 150 K. Electrical resistivity data suggest $Cr_{2.76}Te_4$ to be metallic throughout the measured temperature range with a *kink* at around 50 K due to antiferromagnetic (AFM) ordering. Our studies clearly point to $Cr_{2.76}Te_4$ as an itinerant ferromagnet. Magnetotransport measurements demonstrate large anomalous Hall effect (AHE) and topological Hall effect (THE) in this system. First-principles calculations point to an intrinsic AHE due to nonzero Berry curvature near the Fermi level, while experimentally it is found to be an extrinsic AHE due to the skew scattering [28].

II. EXPERIMENTAL DETAILS

High-quality single crystals of $Cr_{2.76}Te_4$ were grown by the chemical vapor transport technique with iodine as a transport

---

*setti@bose.res.in

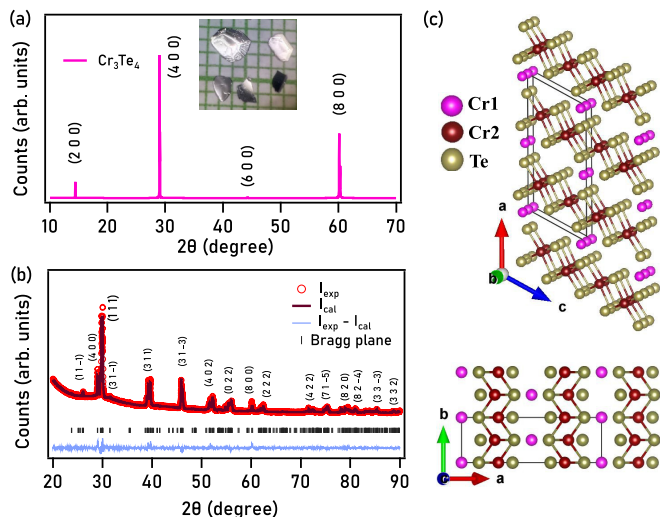FIG. 1. (a) XRD pattern from $Cr_{2.76}Te_4$ single crystals. Inset in (a) shows the photographic image of the single crystals. (b) X-ray diffraction pattern from the crushed $Cr_{2.76}Te_4$ single crystals, overlapped with Rietveld refinement. (c) Schematic crystal structure of $Cr_{2.76}Te_4$ obtained from the Rietveld refinement.

agent as per the procedure described earlier [29]. Excess iodine present on the crystals was removed by washing with ethanol several times and dried under vacuum. The as-grown single crystals were large in size (3×2 mm^2), were looking shiny, and easily cleavable in the bc plane. A photographic image of typical single crystals is shown in the inset of Fig. 1(a). Crystal structural and phase purity of the single crystals were identified by the x-ray diffraction (XRD) technique using a Rigaku x-ray diffractometer (SmartLab; 9 kW) with Cu $K\alpha$ radiation of wavelength 1.540 59 Å. A compositional analysis of the single crystals was done using the energy dispersive x-ray spectroscopy (EDXS). Magnetic and transport studies were carried out on the physical property measurement system (9 Ta physical property measurement system; DynaCool, Quantum Design). See Supplemental Material for more discussion on the chemical composition of the studied system [30]. Electrical resistivity and Hall measurements were performed in the standard four-probe method. To eliminate the longitudinal magnetoresistance contribution due to voltage probe misalignment, the Hall resistance was calculated as $\rho_{yz}(H) = [\rho_{yz}(+H) - \rho_{yz}(-H)]/2$.

III. DENSITY FUNCTIONAL THEORY CALCULATIONS

We have performed density functional theory (DFT) calculations using the QUANTUM ESPRESSO package [31,32]. We used fully relativistic pseudopotentials in order to include the spin-orbit interaction. Generalized gradient approximation was considered based on Perdew-Burke-Ernzerhof implementation [33] within the projector augmented wave basis [34]. For wave function and charge density expansions, cutoff values of 50 and 300 Ry were chosen, respectively. For the self-consistent calculation, a $7 \times 7 \times 7$ Monkhorst-Pack grid was used [35]. In order to consider the van der Waals forces, semiempirical Grimme's DFT-D2 correction [36] was included. We further constructed a tight-binding

model based on the maximally localized Wannier functions using the WANNIER90 code [37], with Cr $3d$, Cr $3s$, Te $5p$, and Te $5s$ orbitals as the basis. Then utilizing the as-obtained tight-binding model, we calculated Berry curvature along the high-symmetry directions using the Kubo formula [38] encoded in the WANNIER90 code [37]. We have calculated intrinsic anomalous Hall conductivity (AHC) by integrating the x component of Berry curvature over the entire Brillouin zpne using the WANNIERTOOLS code [39].

IV. RESULTS AND DISCUSSION

Figure 1(a) shows the XRD pattern of $Cr_{2.76}Te_4$ single crystal with intensity peaks of ($l\,0\,0$) Bragg plane, indicating that the crystal growth plane is along the a axis. The inset in Fig. 1(a) shows the photographic image of $Cr_{2.76}Te_4$ single crystal. Figure 1(b) shows an XRD pattern of crushed $Cr_{2.76}Te_4$ single crystals measured at room temperature. All peaks in the XRD pattern can be attributed to the monoclinic crystal structure of the $C12/m1$ space group (No. 12) without any impurity phases, consistent with the crystal phase of Cr_3Te_4 [40]. Rietveld refinement confirms the monoclinic structure with lattice parameters $a = 13.9655(2)$ Å, $b = 3.9354(4)$Å, $c = 6.8651(7)$ Å, $\alpha = \beta = 90°$, and $\gamma = 118.326(7)°$. These values are in good agreement with previous reports on similar systems [41,42]. Figure 1(c) shows the schematic crystal structure of $Cr_{2.76}Te_4$ projected onto the ac plane (top panel) and the ab plane (bottom panel). Cr1 atoms are located in the Cr-vacant layer with an occupancy of 0.189/u.c., whereas Cr2 atoms are located in the Cr-full layer with an occupancy of 0.5/u.c. The intercalated Cr atoms (Cr1) are sandwiched within the van der Waals gap created by the two $CrTe_2$ layers, as shown in Fig. 1(c). The EDXS measurements suggest an actual chemical composition of $Cr_{2.76}Te_4$.

To explore the magnetic properties of $Cr_{2.76}Te_4$, magnetization as a function of temperature $[M(T)]$ was measured as shown in Fig. 2(a) at a field of 1000 Oe applied parallel to the bc plane ($H \parallel bc$) and the a axis ($H \parallel a$) for both zero-field-cooled (ZFC) and field-cooled (FC) modes. We observe that $Cr_{2.76}Te_4$ exhibits paramagnetic to ferromagnetic (FM) transition at a Curie temperature (T_C) of 310 K, which is close to the Curie temperature of Cr_3Te_4 ($T_C = 316$ K). A decrease in the sample temperature results in a decrease in the magnetization for both $H \parallel bc$ and $H \parallel a$ at around 50 K, possibly due to spin canting emerged from the coupling between in-plane (bc plane) AFM order and out-of-plane (a axis) FM orders [43,44]. Also, the in-plane saturated magnetic moment of $1.78\mu_B$/Cr is almost four times higher than the out-of-plane saturated magnetic moment of $0.43\mu_B$/Cr at 2 K with an applied field of 1000 Oe, clearly demonstrating strong magnetocrystalline anisotropy in $Cr_{2.76}Te_4$. From the magnetization difference between ZFC and FC, $\Delta M = M_{FC} - M_{ZFC}$, shown in Fig. 2(b), we notice significant magnetization fluctuations as the maximum of ΔM varies between in-plane and out-of-plane directions in going from 50 to 150 K [45].

The magnetic state of $Cr_{2.76}Te_4$ is further explored by measuring the magnetization isotherms $[M(H)]$ for $H \parallel a$ and $H \parallel bc$ at various sample temperatures as shown in Figs. 2(c) and 2(d), respectively. Consistent with $M(T)$ data, the
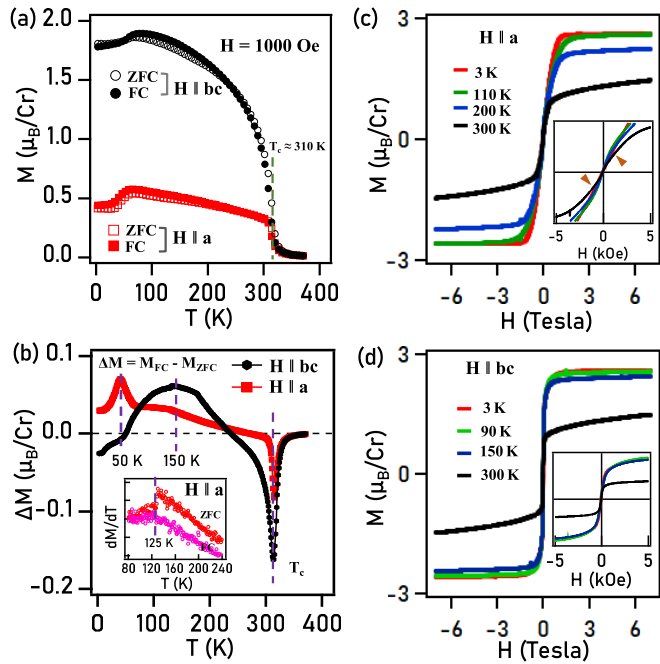
FIG. 2. (a) Temperature-dependent magnetization $M(T)$ measured under ZFC and FC modes with a magnetic field $H = 1000$ Oe for $H \parallel a$ and $H \parallel bc$. (b) Variation of magnetization $\Delta M = (M_{FC}-M_{FC})$ plotted as a function of temperature. Inset in (b) shows the first derivative of magnetization with respect to the temperature (dM/dT) of the data shown in (a) for $H \parallel a$. (c) and (d) Field-dependent magnetization $M(H)$ measured at different temperatures for $H \parallel a$ and $H \parallel bc$, respectively.

magnetization saturation occurs at an applied field of 0.7 and 1.4 T for $H \parallel bc$ and $H \parallel a$, respectively, suggesting the bc plane to be the easy-magnetization plane. Also, $Cr_{2.76}Te_4$ is a soft ferromagnet as it has a negligible coercivity [see Fig. S1(a) in the Supplemental Material [30]]. The observed saturation magnetization (M_s) 2.586 μ_B/Cr and 2.55 μ_B/Cr for $H \parallel a$ and $H \parallel bc$, respectively, is smaller than the stand-alone Cr atom (3 μ_B), indicating correlated magnetic states in $Cr_{2.76}Te_4$. These observations are in good agreement with the report on $Cr_{2.76}Te_4$ [46].

Next, coming to the main results of this contribution, Fig. 3(a) exhibits the temperature-dependent longitudinal electrical resistivity (ρ_{zz}) of $Cr_{2.76}Te_4$. $\rho_{zz}(T)$ suggests a metallic nature throughout the measured temperature range [47]. However, a kink at around 50 K is noticed in the resistivity, related to the AFM ordering [see Fig. 2(a)]. The bottom inset of Fig. 3(a) depicts a schematic diagram of linear-four-probe measuring geometry and the top inset elucidates the quadratic nature of low-temperature resistivity up to 50 K as can be explained well by the Fermi liquid theory, $\rho(T) = \rho_0 + aT^2$ where ρ_0 is the temperature-independent residual resistivity. Schematic diagram of Hall measuring geometry is shown in Fig. 3(b). The Hall resistivity, ρ_{yz}, is measured with current along the y axis and magnetic field applied along the x axis to get the Hall voltage along the z axis. Thus, Fig. 3(c) shows field-dependent Hall resistivity ρ_{yz} (black curve) measured at various sample temperatures. The total Hall resistivity (ρ_{yz}) may have contributions from the normal Hall effect (ρ^N) and the anomalous Hall effect (ρ^A). Thus, the total Hall resistivity can be expressed by the empirical
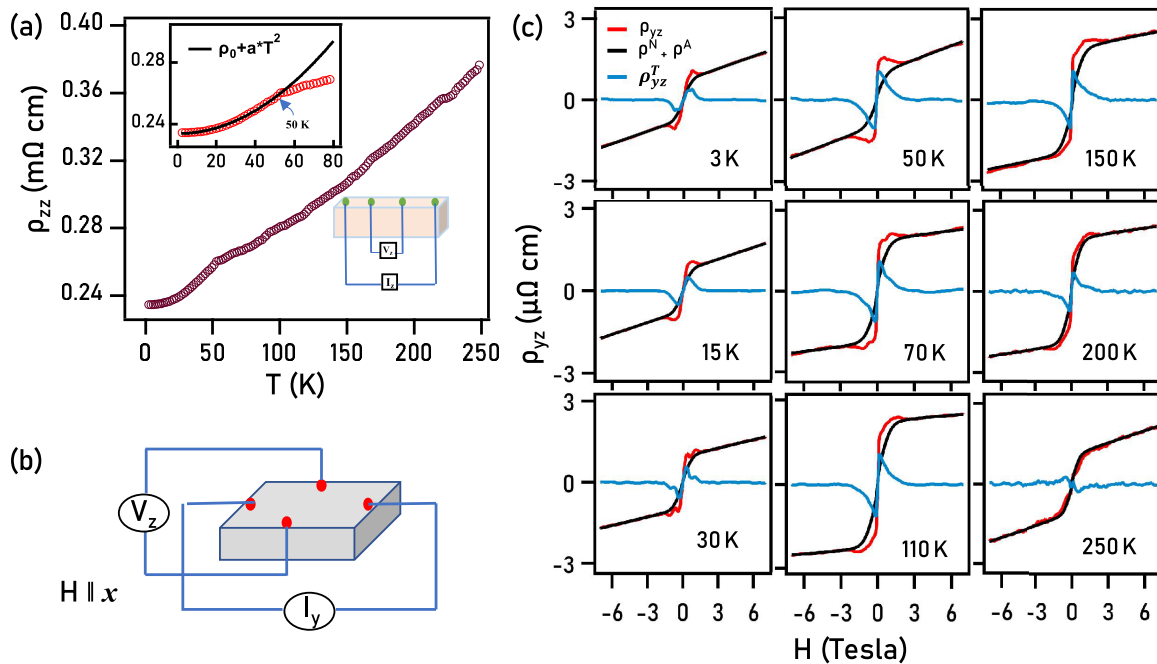

FIG. 3. (a) Temperature-dependent longitudinal resistivity $\rho_{zz}(T)$. The top inset in (a) shows low-temperature resistivity fitted by $\rho(T) = \rho_0 + bT^2$ and the bottom inset in (a) shows a schematic diagram of linear-four-probe contacts. (b) Hall measuring geometry is shown schematically. (c) Hall resistivity (ρ_{yz}) plotted as a function of magnetic field measured at various temperatures. In (c), red curves represent the experimental data of total Hall resistivity (ρ_{yz}), black curves represent the contributions from the normal and anomalous Hall resistivities $(\rho^N + \rho^A)$, and blue curves represent the topological Hall resistivity (ρ_{yz}^T). See the text for more details.
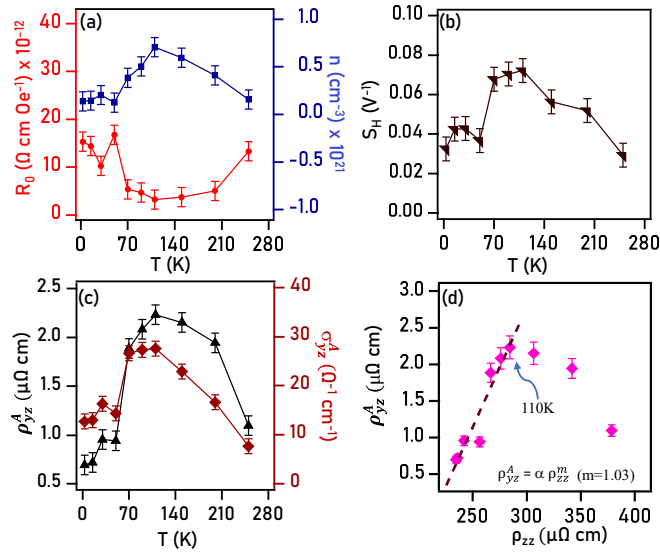
FIG. 4. Temperature dependence of (a) Normal Hall coefficient R_0 (left axis) and charge carrier density n (right axis). (b) Anomalous Hall scaling coefficient S_H plotted as a function of temperature. (c) Anomalous Hall resistivity (ρ_{yz}^A) and Hall conductivity (σ_{yz}^A). (d) Plot of ρ_{yz}^A *vs.* ρ_{zz}. Dashed line in (d) is linear fitting with equation shown on the figure.

formula, $\rho_{yz}(H) = \rho^N(H) + \rho^A(H) = \mu_0 R_0 H + \mu_0 R_S M$, where R_0 and R_S are the normal and anomalous Hall coefficients, respectively. These coefficients can be obtained by performing a linear fit using the relation $\frac{\rho_{yz}}{\mu_0 H} = R_0 + R_S \frac{M}{H}$ as shown in Fig. S1(c) of the Supplemental Material [30]. Having obtained the normal and anomalous Hall coefficients, we can now fit the total Hall resistivity (red curves) using the equation $\rho_{yz}(H) = \mu_0 R_0 H + \mu_0 R_s M$. The fitting should be nearly perfect if there is no topological Hall contribution. However, from Fig. 3(c) we can clearly notice that the fitting (red curve) is not perfect. Therefore, the topological Hall resistivity also contributes to the total Hall resistivity, which can be expressed by $\rho_{yz}(H) = \rho^N(H) + \rho^A(H) + \rho^T(H)$. Thus, the topological Hall contribution (blue curve) is extracted using the relation $\rho^T(H) = \rho_{yz}(H) - [\rho^N(H) + \rho^A(H)]$ [48–50]. See the Supplemental Material for more details [30].

Figure 4(a) depicts the normal Hall coefficient (R_0) and the charge-carrier density (n) derived using the formula $R_0 = 1/n|e|$, plotted as a function of temperature. We clearly notice from Fig. 4(a) that as the temperature decreases the carrier density increases up to 110 K. However, below 110 K, the carrier density decreases with temperature and gets saturated below 50 K. Figure 4(b) (left axis) presents the anomalous Hall resistivity (ρ_{yz}^A) at zero field obtained by linearly intersecting the field axis [see Fig. 3(c)]. The maximum anomalous Hall resistivity is noticed at around 110 K. Anomalous Hall conductivity, σ_{yz}^A, derived using the formula $\sigma_{yz}^A = \frac{\rho_{yz}}{\rho_{yz}^2 + \rho_{zz}^2}$, is shown in the right axis of Fig. 4(c), again to find the maximum Hall conductivity of $\sigma_{yz}^A = 27 \ \Omega^{-1} \text{cm}^{-1}$ at around 110 K. Figure 4(b) shows anomalous scaling coefficient $S_H = \frac{\rho_{yz}^A}{M \rho_{zz}^2}$, plotted as a function of temperature. The values of

S_H are in line with the itinerant ferromagnetic systems of $S_H = 0.01$–$0.2 \ \text{V}^{-1}$ [51]. In general, anomalous Hall effect can occur in solids either intrinsically originated from the nonzero-Berry curvature in the momentum space [52,53] or extrinsically due to side-jump/skew-scattering mechanisms [28,52,54]. Therefore, to elucidate the mechanism of AHE in $Cr_{2.76}Te_4$, we plotted ρ_{yz}^A vs ρ_{zz} as shown in Fig. 4(d). From Fig. 4(d) it is evident that ρ_{yz}^A linearly changes with ρ_{zz} ($\rho_{yz} = \alpha \rho_{zz}^m$ for $m = 1.03 \pm 0.02$) up to 110 K and then deviates on further increasing the sample temperature [55]. In the case of the itinerant ferromagnetic system, the Hall resistivity can be expressed by the relation $\rho_{yz} = \alpha \rho_{zz} + \beta \rho_{zz}^2$ where α and β are the skew-scattering and side-jump terms, respectively [47,56,57]. That means, in the case of skew scattering, ρ_{yz}^A linearly depends on ρ_{zz}, while ρ_{yz}^A quadratically depends on ρ_{zz} in the case of side jump. Since the Hall resistivity (ρ_{yz}) linearly depends on ρ_{zz}, the skew scattering could be the most suitable mechanism of AHE observed in this system [47,58]. Note that the intrinsic Berry curvature contribution to the anomalous Hall resistance (AHR) also quadratically depends on ρ_{zz} [55]. To make a point, it looks like 110 K is the critical temperature of the properties discussed in Figs. 4(a)–4(d). However, as per the dM/dT data shown in the inset of Fig. 2(b), we think that the critical temperature could be ≈ 125 K instead of 110 K as we can see a significant change in magnetization across ≈ 125 K.

Our experimental findings on the AHE have been examined using the density functional theory calculations as presented in Fig. 5. For the calculations, we considered a primitive unit cell of Cr_3Te_4, consisting of three Cr (one Cr1 and two Cr2 type) and four Te atoms. The magnetic spins of Cr atoms were considered along the x direction. Our calculations suggest a ferromagnetic ground state with average magnetic moments of 3.23 μ_B and 3.15 μ_B per Cr1 and Cr2 atoms, respectively, slightly higher than the experimental average value of 2.568 μ_B/Cr. In Fig. 5(b), we present the bulk electronic band structure of Cr_3Te_4. The system is found to be metallic with several bands crossing the Fermi level (E_F). Several band crossing points are found near E_F along C_2-Y_2, D_2-A, A-Γ, and L_2-Γ k paths, but slightly away from the high-symmetry points. Next, we explore the Berry curvature (Ω) calculated using the formula $\Omega(k) = \nabla(k) \times A(k)$ [where $A(k)$ is the Berry connection]. Variation of the x component of Berry curvature (Ω^x) at E_F along the high-symmetry k path is shown in Fig. 5(c). We can notice from Fig. 5(c) that Ω^x is strongly enhanced along the A-Γ (k_z) direction. Further, Fig. 5(d) shows the AHC, σ_{yz}, of Cr_3Te_4 calculated as a function of energy using Eq. (1):

$$\sigma_{yz} = \frac{e^2}{\hbar} \int f[\epsilon_n(\mathbf{k})] \Omega_n^x(\mathbf{k}) \frac{d\mathbf{k}}{(2\pi)^3}, \qquad (1)$$

where $f[\epsilon_n(\mathbf{k})]$ is the Fermi-Dirac distribution function.

Our calculations suggest an intrinsic AHC of $\sigma_{yz} \approx 260 \ \Omega^{-1} \text{cm}^{-1}$ near E_F, much larger than the experimental value of $\sigma_{yz}^A = 27 \ \Omega^{-1} \text{cm}^{-1}$. Such a small AHC suggests a dominant impurity scattering contribution to the total anomalous Hall effect of Cr_3Te_4 [59], i.e., the skew-scattering contribution in the dirty limit [60]. However, despite that the system is in the dirty limit, the total AHC should
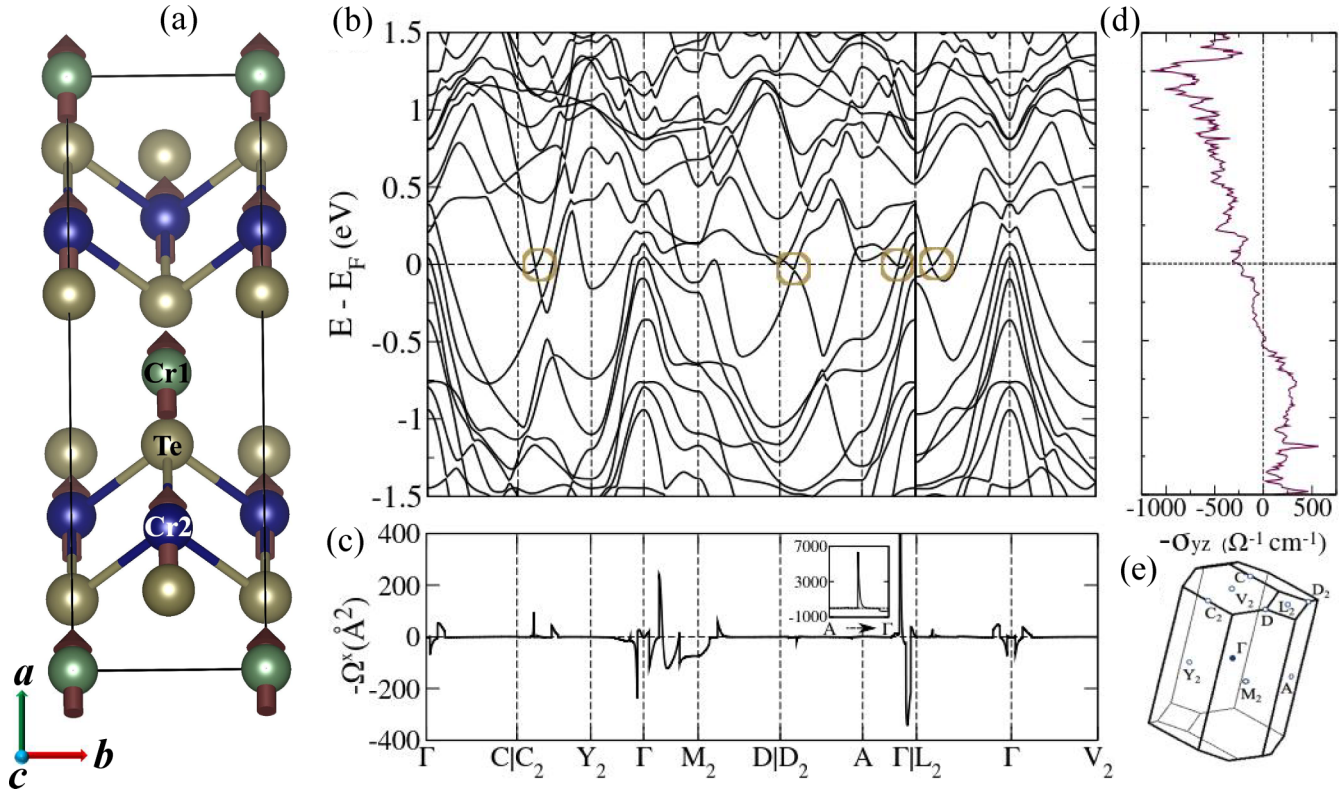
FIG. 5. (a) Schematic monoclinic unit cell of $Cr_{2.76}Te_4$. (b) Electronic band structure of $Cr_{2.76}Te_4$ calculated with the inclusion of spin-orbit coupling. In (b) the Weyl points near the Fermi level are encircled. (c) x component of the Berry curvature, Ω^x, calculated at the Fermi level. Inset in (c) shows a zoomed-in view of Ω^x for the A-Γ segment. (d) Anomalous Hall conductivity, σ_{yz}, plotted as a function of energy. (e) High-symmetry points defined on the Brillouin zone of the monoclinic primitive unit cell.

be at least comparable to the value of the intrinsic AHC ($\approx 260\ \Omega^{-1}\ cm^{-1}$) as it has contributions from both intrinsic Berry curvature and extrinsic skew scattering. In contrast, experimentally, we find a much smaller AHC compared to theoretical calculations. Note here that the calculations performed on the stoichiometric Cr_3Te_4 predict a large intrinsic AHC near E_F due to the presence of several band crossing points (Weyl points). But the intrinsic AHC rapidly decreases as we move away from E_F. This is particularly true when E_F is shifted to lower binding energies [see Fig. 5(d)]. Therefore, a genuine reason behind the discrepancy of AHC between experiment and theory could be that the experiments are performed on a slightly off-stoichiometric composition of $Cr_{2.76}Te_4$ with 8% Cr deficiency per formula unit, shifting the Fermi level towards the lower binding energy. The xaximum topological Hall resistivity (ρ_{max}^T) is plotted as a function of temperature in Fig. 6(a) by the black data points. Also, the green data points in Fig. 6(a) represent the magnetocrystalline anisotropy constant K_u calculated using Eq. (2):

$$K_u = \mu_0 \int_0^{M_s} [H_{bc}(M) - H_a(M)]\, dM. \qquad (2)$$

Here, M_s represents saturation magnetization. H_{bc} and H_a represent $H \parallel bc$ and $H \parallel a$, respectively.

From Fig. 6(a), we can notice that the topological Hall resistivity is highest within the temperature range of 50–150 K. Also, most importantly, the temperature dependence of K_u resembles ρ_{max}^T. In Fig. 6(b), the black data points illustrate

the temperature-dependent saturation field (H_s) beyond which the system becomes ferromagnetic [extracted from Fig. 2(c)] and the red data points illustrate the temperature-dependent field (H_T) beyond which ρ_{yz}^T becomes zero [extracted from Fig. 3(c)]. Interestingly, both fields H_T and H_s perfectly overlap at all measured temperatures. This can be understood using the schematics shown in Fig. 6(c). This means, at a given temperature up to the saturation field ($H < H_s$), the system possesses a noncoplanar spin structure and hence shows the topological Hall effect [61]. However, for the applied field beyond magnetic saturation ($H > H_s$), the system becomes ferromagnetic and thus THE disappears.

Further, the maximum topological Hall resistivity $\rho_{max}^T \approx 1.1\ \mu\Omega\ cm$ over a broad temperature range of 50 K $< T <$ 150 K observed in this vdW ferromagnetic $Cr_{2.76}Te_4$ is in the same order of magnitude found in the chiral semimetals such as Mn_2PtSn [62], Gd_3PdSi_3 [63], $LaMn_2Ge_2$ [64], and in other Cr_xTe_y based systems [23,26]. Interestingly, so far THE is observed in Cr_xTe_y systems in their hexagonal (trigonal) crystal structure [23,26,65] but not in the monoclinic structure that we found in the present study. As discussed above, the easy axis of magnetization in $Cr_{2.76}Te_4$ is found to be in the bc plane and thus for small applied fields the Cr spins are canted out of the bc plane towards the a axis for $H \parallel a$. In this way, the noncoplanar spin structure has been generated for sufficiently smaller fields [23,26,64–67].

Several mechanisms are proposed to understand the topological Hall effect, such as the antisymmetric exchange
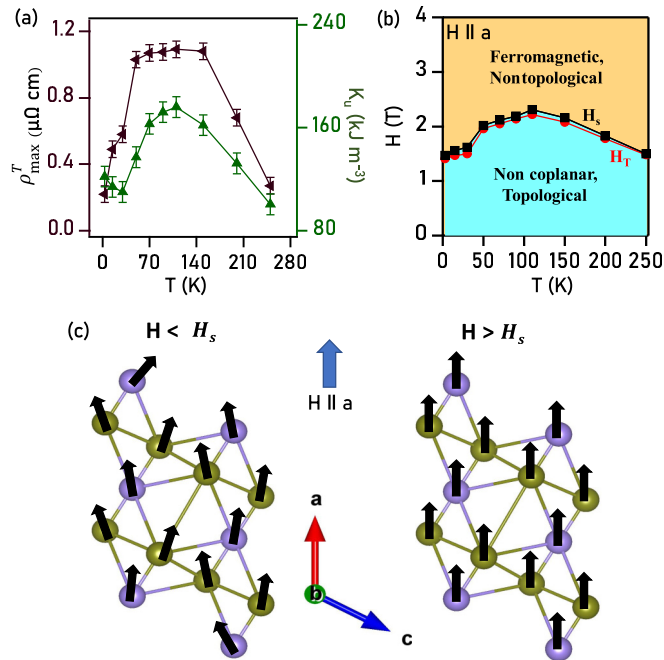
FIG. 6. (a) Maximum value of ρ_{max}^T and magnetocrystalline anisotropy (K_u) plotted as a function of temperature. (b) Saturation magnetic field (H_s) and magnetic field (H_T) above which the topological Hall effect disappears for $H \parallel a$. (c) Schematic representation of the Cr spin configuration for $H < H_s$ (left) and $H > H_s$. See the text for more details.

or Dzyaloshinskii-Moriya interaction in the noncentrosymmetric systems [68–70] and the uniaxial magnetocrystalline anisotropy in the centrosymmetric systems [71–74]. In the case of monoclinic Cr_3Te_4 ($C21/m1$), which is a centrosymmetric crystal, the chiral-spin structure could be stabilized by the strong MCA. This analogy is completely supported by our experimentally estimated MCA values at various temperatures as shown in Fig. 6(a). Most importantly, the highest ρ_{max}^T value has been obtained at the highest magnetocrystalline anisotropy of $K_u = 165$ kJ/m^3. This is because, in the presence of the chiral-spin structure, the itinerant electrons

acquire real-space Berry curvature associated with finite scalar-spin chirality $\chi_{ijk} = S_i(S_j \times S_k)$, which serves as a fictitious magnetic field to generate the topological Hall signal [75–77].

V. CONCLUSIONS

To summarize, we have grown high-quality single crystals of layered ferromagnetic $Cr_{2.76}Te_4$ in the monoclinic phase to study the electrical transport, Hall effect, and magnetic properties. Our studies suggest $Cr_{2.76}Te_4$ to be a soft ferromagnet with a negligible coercivity. The easy axis of magnetization is found to be parallel to the *bc* plane, leading to strong magnetocrystalline anisotropy. Below 50 K, an antiferromagneticlike transition is noticed. Interestingly, in going from 50 to 150 K the strength of magnetic moment switches between out of plane and in plane, suggests fluctuating Cr spins. From the electrical resistivity measurements the system is found to be metallic throughout the measured temperature range. Also, a kink at around 50 K due to AFM ordering is noticed. Magnetotransport measurements demonstrate large AHE and THE in this system. First-principles calculations point to an intrinsic AHE due to nonzero Berry curvature near the Fermi level, while experimentally it is found to be an extrinsic AHE due to skew scattering. Topological Hall effect has been observed due to the noncoplanar spin structure in the presence of strong magnetocrystalline anisotropy.

[1] M. Augustin, S. Jenkins, R. F. Evans, K. S. Novoselov, and E. J. Santos, Properties and dynamics of meron topological spin textures in the two-dimensional magnet CrCl$_3$, Nat. Commun. **12**, 185 (2021).

[2] L. Chen, J.-H. Chung, M. B. Stone, A. I. Kolesnikov, B. Winn, V. O. Garlea, D. L. Abernathy, B. Gao, M. Augustin, E. J. G. Santos, and P. Dai, Magnetic Field Effect on Topological Spin Excitations in CrI$_3$, Phys. Rev. X **11**, 031047 (2021).

[3] K. Choudhary, K. F. Garrity, J. Jiang, R. Pachter, and F. Tavazza, Computational search for magnetic and non-magnetic 2D topological materials using unified spin–orbit spillage screening, npj Comput. Mater. **6**, 49 (2020).

[4] N. Nagaosa and Y. Tokura, Topological properties and dynamics of magnetic skyrmions, Nat. Nanotechnol. **8**, 899 (2013).

[5] J. R. Schaibley, H. Yu, G. Clark, P. Rivera, J. S. Ross, K. L. Seyler, W. Yao, and X. Xu, Valleytronics in 2D materials, Nat. Rev. Mater. **1**, 16055 (2016).

[6] A. Fert, N. Reyren, and V. Cros, Magnetic skyrmions: Advances in physics and potential applications, Nat. Rev. Mater. **2**, 17031 (2017).

[7] C. Gong, L. Li, Z. Li, H. Ji, A. Stern, Y. Xia, T. Cao, W. Bao, C. Wang, Y. Wang *et al.*, Discovery of intrinsic ferromagnetism in two-dimensional van der Waals crystals, Nature (London) **546**, 265 (2017).

[8] K. L. Seyler, D. Zhong, D. R. Klein, S. Gao, X. Zhang, B. Huang, E. Navarro-Moratalla, L. Yang, D. H. Cobden, M. A. McGuire *et al.*, Ligand-field helical luminescence in a 2D ferromagnetic insulator, Nat. Phys. **14**, 277 (2018).

[9] Z. Fei, B. Huang, P. Malinowski, W. Wang, T. Song, J. Sanchez, W. Yao, D. Xiao, X. Zhu, A. F. May *et al.*, Two-dimensional itinerant ferromagnetism in atomically thin Fe_3GeTe_2, Nat. Mater. **17**, 778 (2018).

[10] N. D. Mermin and H. Wagner, Absence of Ferromagnetism or Antiferromagnetism in One- or Two-Dimensional Isotropic Heisenberg Models, Phys. Rev. Lett. **17**, 1133 (1966).

[11] B. Huang, G. Clark, E. Navarro-Moratalla, D. R. Klein, R. Cheng, K. L. Seyler, D. Zhong, E. Schmidgall, M. A. McGuire, D. H. Cobden, W. Yao, D. Xiao, P. Jarillo-Herrero, and X. Xu, Layer-dependent ferromagnetism in a van der Waals crystal down to the monolayer limit, Nature (London) **546**, 270 (2017).

[12] K. S. Burch, D. Mandrus, and J.-G. Park, Magnetism in two-dimensional van der Waals materials, Nature (London) **563**, 47 (2018).

[13] C. Gong and X. Zhang, Two-dimensional magnetic crystals and emergent heterostructure devices, Science **363**, eaav4450 (2019).

[14] M.-G. Han, J. A. Garlow, Y. Liu, H. Zhang, J. Li, D. DiMarzio, M. W. Knight, C. Petrovic, D. Jariwala, and Y. Zhu, Topological magnetic-spin textures in two-dimensional van der Waals $Cr_2Ge_2Te_6$, Nano Lett. **19**, 7859 (2019).

[15] Y. You, Y. Gong, H. Li, Z. Li, M. Zhu, J. Tang, E. Liu, Y. Yao, G. Xu, F. Xu, and W. Wang, Angular dependence of the topological Hall effect in the uniaxial van der Waals ferromagnet Fe_3GeTe_2, Phys. Rev. B **100**, 134441 (2019).

[16] Y. Gao, S. Yan, Q. Yin, H. Huang, Z. Li, Z. Zhu, J. Cai, B. Shen, H. Lei, Y. Zhang, and S. Wang, Manipulation of topological spin configuration via tailoring thickness in van der Waals ferromagnetic $Fe_{5-x}GeTe_2$, Phys. Rev. B **105**, 014426 (2022).

[17] M. Schmitt, T. Denneulin, A. Kovács, T. G. Saunderson, P. Rüßmann, A. Shahee, T. Scholz, A. H. Tavabi, M. Gradhand, P. Mavropoulos *et al.*, Skyrmionic spin structures in layered Fe_5GeTe_2 up to room temperature, Commun. Phys. **5**, 254 (2022).

[18] Y. Zhu, X. Kong, T. D. Rhone, and H. Guo, Systematic search for two-dimensional ferromagnetic materials, Phys. Rev. Mater. **2**, 081001(R) (2018).

[19] Y. Liu and C. Petrovic, Critical behavior of the quasi-two-dimensional weak itinerant ferromagnet trigonal chromium telluride $Cr_{0.62}Te$, Phys. Rev. B **96**, 134410 (2017).

[20] T. Eto, M. Ishizuka, S. Endo, T. Kanomata, and T. Kikegawa, Pressure-induced structural phase transition in a ferromagnet CrTe, J. Alloys Compd. **315**, 16 (2001).

[21] F. Wang, J. Du, F. Sun, R. F. Sabirianov, N. Al-Aqtash, D. Sengupta, H. Zeng, and X. Xu, Ferromagnetic Cr_2Te_3 nanorods with ultrahigh coercivity, Nanoscale **10**, 11028 (2018).

[22] B. Hessen, T. Siegrist, T. Palstra, S. Tanzler, and M. Steigerwald, Hexakis (triethylphosphine) octatelluridohexachromium and a molecule-based synthesis of chromium telluride, Cr_3Te_4, Inorg. Chem. **32**, 5165 (1993).

[23] Y. Wang, J. Yan, J. Li, S. Wang, M. Song, J. Song, Z. Li, K. Chen, Y. Qin, L. Ling, H. Du, L. Cao, X. Luo, Y. Xiong, and Y. Sun, Magnetic anisotropy and topological Hall effect in the trigonal chromium tellurides Cr_5Te_8, Phys. Rev. B **100**, 024434 (2019).

[24] J. Dijkstra, H. H. Weitering, C. F. van Bruggen, C. Haas, and R. A. de Groot, Band-structure calculations, and magnetic and transport properties of ferromagnetic chromium tellurides (CrTe, Cr_3Te_4, Cr_2Te_3), J. Phys.: Condens. Matter **1**, 9141 (1989).

[25] H. Ipser, K. L. Komarek, and K. O. Klepp, Transition metal-chalcogen systems VIII: The CrTe phase diagram, J. Less-Common Met. **92**, 265 (1983).

[26] M. Huang, L. Gao, Y. Zhang, X. Lei, G. Hu, J. Xiang, H. Zeng, X. Fu, Z. Zhang, G. Chai *et al.*, Possible topological Hall effect above room temperature in layered $Cr_{1.2}Te_2$ ferromagnet, Nano Lett. **21**, 4280 (2021).

[27] J. Liu, B. Ding, J. Liang, X. Li, Y. Yao, and W. Wang, Magnetic skyrmionic bubbles at room temperature and sign reversal of the topological Hall effect in a layered ferromagnet $Cr_{0.87}Te$, ACS Nano **16**, 13911 (2022).

[28] J. Smit, The spontaneous Hall effect in ferromagnetics II, Physica **24**, 39 (1958).

[29] T. Hashimoto, K. Hoya, M. Yamaguchi, and I. Ichitsubo, Magnetic properties of single crystals $Cr_{2-\delta}Te_3$, J. Phys. Soc. Jpn. **31**, 679 (1971).

[30] See Supplemental Material at http://link.aps.org/supplemental/10.1103/PhysRevMaterials.7.094204 for topological Hall resistivity analysis.

[31] P. Giannozzi, S. Baroni, N. Bonini, M. Calandra, R. Car, C. Cavazzoni, D. Ceresoli, G. L. Chiarotti, M. Cococcioni, I. Dabo *et al.*, QUANTUM ESPRESSO: A modular and open-source software project for quantum simulations of materials, J. Phys.: Condens. Matter **21**, 395502 (2009).

[32] P. Giannozzi, O. Andreussi, T. Brumme, O. Bunau, M. B. Nardelli, M. Calandra, R. Car, C. Cavazzoni, D. Ceresoli, M. Cococcioni *et al.*, Advanced capabilities for materials modelling with Quantum ESPRESSO, J. Phys.: Condens. Matter **29**, 465901 (2017).

[33] J. P. Perdew, K. Burke, and M. Ernzerhof, Generalized Gradient Approximation Made Simple, Phys. Rev. Lett. **77**, 3865 (1996).

[34] P. E. Blöchl, Projector augmented-wave method, Phys. Rev. B **50**, 17953 (1994).

[35] H. J. Monkhorst and J. D. Pack, Special points for Brillouin-zone integrations, Phys. Rev. B **13**, 5188 (1976).

[36] S. Grimme, Semiempirical GGA-type density functional constructed with a long-range dispersion correction, J. Comput. Chem. **27**, 1787 (2006).

[37] A. A. Mostofi, J. R. Yates, Y.-S. Lee, I. Souza, D. Vanderbilt, and N. Marzari, wannier90: A tool for obtaining maximally-localised Wannier functions, Comput. Phys. Commun. **178**, 685 (2008).

[38] D. J. Thouless, M. Kohmoto, M. P. Nightingale, and M. den Nijs, Quantized Hall Conductance in a Two-Dimensional Periodic Potential, Phys. Rev. Lett. **49**, 405 (1982).

[39] Q. Wu, S. Zhang, H.-F. Song, M. Troyer, and A. A. Soluyanov, WannierTools: An open-source software package for novel topological materials, Comput. Phys. Commun. **224**, 405 (2018).

[40] M. Yamaguchi and T. Hashimoto, Magnetic Properties of Cr_3Te_4 in Ferromagnetic Region, J. Phys. Soc. Jpn. **32**, 635 (1972).

[41] S. Ohta, Magnetic properties of $(Cr_{1-u}V_u)_3Te_4$, J. Phys. Soc. Jpn. **54**, 1076 (1985).

[42] D. Babot, M. Wintenberger, B. Lambert-Andron, and M. Chevreton, Propriétés magnétiques et conductibilité electrique

des composés ternaires $Cr_3Se_{4-x}Te_x$, J. Solid State Chem. **8**, 175 (1973).

[43] C. Li, K. Liu, D. Jiang, C. Jin, T. Pei, T. Wen, B. Yue, and Y. Wang, Diverse thermal expansion behaviors in ferromagnetic $Cr_{1-\delta}Te$ with NiAs-type, defective structures, Inorg. Chem. **61**, 14641 (2022).

[44] L.-Z. Zhang, A.-L. Zhang, X.-D. He, X.-W. Ben, Q.-L. Xiao, W.-L. Lu, F. Chen, Z. Feng, S. Cao, J. Zhang, and J.-Y. Ge, Critical behavior and magnetocaloric effect of the quasi-two-dimensional room-temperature ferromagnet Cr_4Te_5, Phys. Rev. B **101**, 214413 (2020).

[45] P. Chen, C. Zhang, Y. Wang, B. Lv, P. Liu, Y. Tian, J. Ran, C. Gao, Q. Liu, and D. Xue, Topological Hall effect in frustrated B2-ordered $Mn_{0.74}Co_{0.57}Al_{0.69}$ films, Phys. Rev. B **104**, 064409 (2021).

[46] K. Shimada, T. Saitoh, H. Namatame, A. Fujimori, S. Ishida, S. Asano, M. Matoba, and S. Anzai, Photoemission study of itinerant ferromagnet $Cr_{1-\delta}Te$, Phys. Rev. B **53**, 7673 (1996).

[47] Y. Liu and C. Petrovic, Anomalous Hall effect in the trigonal Cr_5Te_8 single crystal, Phys. Rev. B **98**, 195122 (2018).

[48] S. Nakatsuji, N. Kiyohara, and T. Higo, Large anomalous Hall effect in a non-collinear antiferromagnet at room temperature, Nature (London) **527**, 212 (2015).

[49] K. Kuroda, T. Tomita, M.-T. Suzuki, C. Bareille, A. Nugroho, P. Goswami, M. Ochi, M. Ikhlas, M. Nakayama, S. Akebi *et al.*, Evidence for magnetic Weyl fermions in a correlated metal, Nat. Mater. **16**, 1090 (2017).

[50] N. Kanazawa, Y. Onose, T. Arima, D. Okuyama, K. Ohoyama, S. Wakimoto, K. Kakurai, S. Ishiwata, and Y. Tokura, Large Topological Hall Effect in a Short-Period Helimagnet MnGe, Phys. Rev. Lett. **106**, 156603 (2011).

[51] S. N. Kaul, Anomalous Hall effect in nickel and nickel-rich nickel-copper alloys, Phys. Rev. B **20**, 5122 (1979).

[52] N. Nagaosa, J. Sinova, S. Onoda, A. H. MacDonald, and N. P. Ong, Anomalous Hall effect, Rev. Mod. Phys. **82**, 1539 (2010).

[53] C. Zeng, Y. Yao, Q. Niu, and H. H. Weitering, Linear Magnetization Dependence of the Intrinsic Anomalous Hall Effect, Phys. Rev. Lett. **96**, 037204 (2006).

[54] L. Berger, Side-jump mechanism for the Hall effect of ferromagnets, Phys. Rev. B **2**, 4559 (1970).

[55] J. Shen, S. Zhang, T. Liang, J. Wang, Q. Zeng, Y. Wang, H. Wei, E. Liu, and X. Xu, Intrinsically enhanced anomalous Hall conductivity and Hall angle in Sb-doped magnetic Weyl semimetal $Co_3Sn_2S_2$, APL Mater. **10**, 090705 (2022).

[56] Y. Tian, L. Ye, and X. Jin, Proper Scaling of the Anomalous Hall Effect, Phys. Rev. Lett. **103**, 087206 (2009).

[57] Y. Wang, C. Xian, J. Wang, B. Liu, L. Ling, L. Zhang, L. Cao, Z. Qu, and Y. Xiong, Anisotropic anomalous Hall effect in triangular itinerant ferromagnet Fe_3GeTe_2, Phys. Rev. B **96**, 134428 (2017).

[58] Z. Z. Jiang, X. Luo, J. Yan, J. J. Gao, W. Wang, G. C. Zhao, Y. Sun, J. G. Si, W. J. Lu, P. Tong *et al.*, Magnetic anisotropy and anomalous Hall effect in monoclinic single crystal Cr_5Te_8, Phys. Rev. B **102**, 144433 (2020).

[59] Y. Liu, H. Tan, Z. Hu, B. Yan, and C. Petrovic, Anomalous Hall effect in the weak-itinerant ferrimagnet $FeCr_2Te_4$, Phys. Rev. B **103**, 045106 (2021).

[60] S. Onoda, N. Sugimoto, and N. Nagaosa, Intrinsic Versus Extrinsic Anomalous Hall Effect in Ferromagnets, Phys. Rev. Lett. **97**, 126602 (2006).

[61] X. Zheng, X. Zhao, J. Qi, X. Luo, S. Ma, C. Chen, H. Zeng, G. Yu, N. Fang, S. U. Rehman *et al.*, Giant topological Hall effect around room temperature in noncollinear ferromagnet $NdMn_2Ge_2$ single crystal, Appl. Phys. Lett. **118**, 072402 (2021).

[62] Z. Liu, A. Burigu, Y. Zhang, H. M. Jafri, X. Ma, E. Liu, W. Wang, and G. Wu, Giant topological Hall effect in tetragonal Heusler alloy Mn_2PtSn, Scr. Mater. **143**, 122 (2018).

[63] T. Kurumaji, T. Nakajima, M. Hirschberger, A. Kikkawa, Y. Yamasaki, H. Sagayama, H. Nakao, Y. Taguchi, T.-h. Arima, and Y. Tokura, Skyrmion lattice with a giant topological Hall effect in a frustrated triangular-lattice magnet, Science **365**, 914 (2019).

[64] G. Gong, L. Xu, Y. Bai, Y. Wang, S. Yuan, Y. Liu, and Z. Tian, Large topological Hall effect near room temperature in noncollinear ferromagnet $LaMn_2Ge_2$ single crystal, Phys. Rev. Mater. **5**, 034405 (2021).

[65] Y. He, J. Kroder, J. Gayles, C. Fu, Y. Pan, W. Schnelle, C. Felser, and G. H. Fecher, Large topological Hall effect in an easy-cone ferromagnet $Cr_{0.9}B_{0.1}Te$, Appl. Phys. Lett. **117**, 052409 (2020).

[66] H. Li, B. Ding, J. Chen, Z. Li, E. Liu, X. Xi, G. Wu, and W. Wang, Large anisotropic topological Hall effect in a hexagonal non-collinear magnet Fe_5Sn_3, Appl. Phys. Lett. **116**, 182405 (2020).

[67] Q. Wang, Q. Yin, and H. Lei, Giant topological Hall effect of ferromagnetic kagome metal Fe_3Sn_2, Chin. Phys. B **29**, 017101 (2020).

[68] X. Yu, Y. Onose, N. Kanazawa, J. H. Park, J. Han, Y. Matsui, N. Nagaosa, and Y. Tokura, Real-space observation of a two-dimensional skyrmion crystal, Nature (London) **465**, 901 (2010).

[69] W. Jiang, G. Chen, K. Liu, J. Zang, S. G. Te Velthuis, and A. Hoffmann, Skyrmions in magnetic multilayers, Phys. Rep. **704**, 1 (2017).

[70] O. Meshcheriakova, S. Chadov, A. K. Nayak, U. K. Rößler, J. Kübler, G. André, A. A. Tsirlin, J. Kiss, S. Hausdorf, A. Kalache *et al.*, Large Noncollinearity and Spin Reorientation in the Novel Mn_2RhSn Heusler Magnet, Phys. Rev. Lett. **113**, 087203 (2014).

[71] P. K. Rout, P. V. P. Madduri, S. K. Manna, and A. K. Nayak, Field-induced topological Hall effect in the noncoplanar triangular antiferromagnetic geometry of Mn_3Sn, Phys. Rev. B **99**, 094430 (2019).

[72] B. Ding, Z. Li, G. Xu, H. Li, Z. Hou, E. Liu, X. Xi, F. Xu, Y. Yao, and W. Wang, Observation of magnetic skyrmion bubbles in a van der Waals ferromagnet Fe_3GeTe_2, Nano Lett. **20**, 868 (2020).

[73] D. A. Gilbert, B. B. Maranville, A. L. Balk, B. J. Kirby, P. Fischer, D. T. Pierce, J. Unguris, J. A. Borchers, and K. Liu, Realization of ground-state artificial skyrmion lattices at room temperature, Nat. Commun. **6**, 8462 (2015).

[74] M. Nakamura, D. Morikawa, X. Yu, F. Kagawa, T.-h. Arima, Y. Tokura, and M. Kawasaki, Emergence of topological Hall effect in half-metallic manganite thin films by tuning perpendicular magnetic anisotropy, J. Phys. Soc. Jpn. **87**, 074704 (2018).

[75] Y. Machida, S. Nakatsuji, Y. Maeno, T. Tayama, T. Sakakibara, and S. Onoda, Unconventional Anomalous Hall Effect

Enhanced by a Noncoplanar Spin Texture in the Frustrated Kondo Lattice $Pr_2Ir_2O_7$, Phys. Rev. Lett. **98**, 057203 (2007).

[76] Y. Taguchi, Y. Oohara, H. Yoshizawa, N. Nagaosa, and Y. Tokura, Spin chirality, Berry phase, and anomalous Hall effect in a frustrated ferromagnet, Science **291**, 2573 (2001).

[77] H. Wang, Y. Dai, G. M. Chow, and J. Chen, Topological Hall transport: Materials, mechanisms and potential applications, Prog. Mater. Sci. **130**, 100971 (2022).